Results in Chemistry 26 (2026) 103358

Contents lists available at ScienceDirect

Results in Chemistry

journal homepage: www.sciencedirect.com/journal/results-in-chemistry

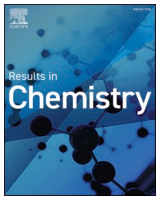

Surfactant-modified ZnO NPs enhance the corrosion barrier performance of PLA coatings on AA2024-T3 aluminum alloy

Budi Mulyati [a,b], Salma Nur Aisyah [a], Saidun Fiddaroini [a], Masruroh [c], Ika Oktavia Wulandari [a], Yuniar Ponco Prananto [a], Norhashila Hashim [d], Akhmad Sabarudin [a,e,*]

[a] Department of Chemistry, Faculty of Science, Universitas Brawijaya, Jl Veteran 12-16, Malang 65145, Indonesia
[b] Department of Aeronautical Engineering, Faculty of Engineering, Nurtanio University, Pajajaran 219, Bandung 40215, Indonesia
[c] Department of Physics, Faculty of Science, Universitas Brawijaya, Jl Veteran 12-16, Malang 65145, Indonesia
[d] Department of Biological and Agricultural Engineering, Faculty of Engineering, Universiti Putra Malaysia, 43400 Serdang, Selangor, Malaysia
[e] Research Center for Advanced System and Material Technology, Universitas Brawijaya, Jl Veteran 12-16, Malang 65145, Indonesia

ARTICLE INFO

Keywords:
ZnO nanoparticles
Surfactant
Corrosion
Aluminum alloy
Coating

ABSTRACT

This work reported the fabrication of ZnO nanoparticles, which were then modified using surfactants to enhance the anticorrosion performance of polylactic acid (PLA) coatings on AA2024-T3 aluminum alloy. Surfactant-modified ZnO nanoparticles were synthesized under alkaline conditions via a precipitation method using cetyltrimethylammonium bromide (CTAB) and polyethylene glycol (PEG) to generate mesoporous structures. BET analysis revealed type IV isotherms with distinct mesoporous features, where ZnO/CTAB exhibited a higher specific surface area (10.63 m^2/g) and smaller mesopore size (~11 nm), while ZnO/PEG produced larger pores (~34 nm) with a lower surface area (3.49 m^2/g). The incorporation of surfactant-modified ZnO into PLA significantly enhanced corrosion resistance in 1 M HCl, with PLA/ZnO/CTAB exhibiting higher inhibition efficiencies (99.36% Tafel; 87.4% EIS) than PLA/ZnO/PEG (99.31% Tafel; 85.3% EIS). Electrochemical analysis indicated a positive shift in corrosion potential, a reduction in corrosion current density, and an increase in charge transfer resistance. Additionally, water contact angle measurements indicated enhanced surface hydrophobicity (>94°), suggesting reduced electrolyte wettability. The enhanced anticorrosion performance is attributed to a synergistic mechanism wherein the presence of mesoporosity facilitates homogeneous nanoparticle dispersion and establishes highly tortuous diffusion pathways, while increased hydrophobicity suppresses electrolyte uptake and ion transport through coating defects. These findings highlight the pivotal role of the interplay between mesoporosity and hydrophobicity as a design principle for the development of high-performance and environmentally benign PLA-based coatings for aerospace aluminum alloys.

1. Introduction

Aluminum alloy (AA2024-T3) is a high performance material widely employed in aerospace applications owing to its excellent strength to weight ratio, high tensile strength, and superior fatigue resistance resulting from appropriate heat treatment processing [1–3]. Its aluminum copper based composition allows extensive use in critical aircraft components, including fuselage skins and wing structures [4,5]. The high copper content in the AA2024-T3 increases its susceptibility to corrosion, particularly in extreme environments [6,7]. Therefore, effective surface protection or coating treatments are crucial to maintain material performance and extend its service life.

Chromate based coatings, although historically effective in protecting AA2024-T3 against corrosion, present significant limitations that restrict their continued application [8]. The primary drawback lies in the high toxicity and carcinogenic nature of hexavalent chromium (Cr (*VI*)), which has prompted stringent environmental regulations and global phase out initiatives [9,10]. Furthermore, as reported by Espinoza-vergara et al. 2024 [11], the self-healing mechanism of chromate coatings relies on the leaching of Cr(VI), which leads to progressive inhibitor depletion and compromised long-term durability, particularly in Cu rich aluminum alloys exposed to aggressive and cyclic environments. The aerospace industry is actively pursuing alternative corrosion protection strategies. Emerging solutions, including non-chromated primers, environmentally benign coatings, and advanced anodizing

* Corresponding author at: Department of Chemistry, Faculty of Science, Universitas Brawijaya, Jl Veteran 12-16, Malang 65145, Indonesia.
E-mail address: sabarjpn@ub.ac.id (A. Sabarudin).

https://doi.org/10.1016/j.rechem.2026.103358
Received 19 February 2026; Accepted 22 April 2026
Available online 23 April 2026

Nomenclature

Chemical compounds and materials

PLA	Polylactic Acid
ZnO	Zinc Oxide
HCl	Hydrochloric Acid
NaOH	Sodium Hydroxide
Cl^-	Chloride Ion
CTAB	Cetyltrimethylammonium Bromide
PEG	Polyethylene Glycol

Electrochemical parameters and variables

R_p	Polarization resistance ($\Omega \cdot cm^2$)
i_{corr}	Corrosion current density (A/cm^2)
E_{corr}	Corrosion potential (V)
a, b	Tafel slopes (mV/decade)
Z'	Real component of impedance (Ω)
Z''	Imaginary component of impedance (Ω)
CPE	Constant Phase Element
f	Frequency (Hz)
IE (%)	Corrosion inhibition efficiency (%) (if applicable)
wt%	Weight percent

Units and constants

Ω	Ohm (electrical resistance)
V	Volt (electrical potential)
A/cm^2	Ampere per square centimeter
mV/decade	Millivolt per logarithmic decade
Hz	Hertz (frequency)
°C	Degrees Celsius
rpm	Revolutions per minute

Techniques and equipment

EIS	Electrochemical Impedance Spectroscopy
Tafel plot	Plot of potential vs. log current density
PP	Potentiodynamic Polarization
SEM	Scanning Electron Microscopy
FTIR	Fourier-Transform Infrared Spectroscopy
XRD	X-ray Diffraction
UV–Vis	UV–Visible Spectroscopy
Autolab	Electrochemical workstation brand used in the study
DropSens	Portable electrochemical analyzer used for EIS and Tafel tests
BET	Brunauer–Emmett–Teller

treatments, have demonstrated significant potential to replace conventional chromate based systems while maintaining effective corrosion resistance [12,13].

Several studies have reported that incorporating oxide nanoparticles such as ZnO, SiO_2, and TiO_2 into polymer matrices can significantly enhance corrosion resistance by strengthening the coating's barrier properties and stabilizing interfacial reactions occurring on the metal surface [14–19]. For example, prior research has demonstrated that combining polymers with NPs yields denser and more mechanically robust films, thereby protecting metal substrates from harsh environments [20,21]. In addition, ZnO containing nanocomposites have been recognized as effective corrosion inhibitors, leveraging ZnO's intrinsic stability and its ability to suppress both anodic and cathodic reactions on metal surfaces [22–24].

One of the most widely used methods for ZnO synthesis is the precipitation method due to its simple process, low cost, and ease of implementation [25,26]. This method allows relatively good control over ZnO particle size and morphology by adjusting synthesis parameters such as precursor concentration, pH, temperature, and reaction time, making it attractive for applications requiring nanomaterials with high surface area [27,28]. The precipitation approach also has inherent limitations, particularly the strong tendency toward particle agglomeration caused by high surface energy, as well as difficulties in achieving narrow size distribution and uniform crystallinity without additional processing steps [29]. Therefore, surfactants or stabilizing agents are commonly employed to overcome these limitations by suppressing agglomeration and improving the stability and dispersion of ZnO NPs [30–32]. The selection of surfactants is critical, as different surfactant types can govern nanoparticle growth, dispersion, and interfacial interactions through distinct mechanisms. Cationic surfactants such as cetyltrimethylammonium bromide (CTAB) provide electrostatic stabilization and can strongly interact with negatively charged species, promoting controlled nucleation and reduced agglomeration [33]. Nonionic surfactants such as polyethylene glycol (PEG) offer steric stabilization, influencing particle growth and enabling the formation of more open and mesoporous structures [34]. Therefore, these two surfactants were selected to systematically compare the influence of electrostatic and steric effects on ZnO nanoparticle characteristics and their subsequent performance in PLA-based anticorrosion coatings.

Studies investigating the use of ZnO NPs synthesized with surfactants on AA2024-T3 remain limited. In fact, adding surfactants during ZnO synthesis can prevent agglomeration, generate mesopores, and produce more uniform NPs. Moreover, PLA is biodegradable and environmentally friendly, making it a promising and more sustainable alternative to conventional inhibitors, while still benefiting from the enhanced protective performance provided by ZnO NPs. The function of the coating on AA2024-T3 is to limit direct contact between the substrate and electrolytes, oxygen, and aggressive ions. The coating can reduce the likelihood of pit initiation and intergranular corrosion, while also slowing the propagation of damage. This protection is particularly important given the widespread use of AA2024-T3 in aircraft structures, as it can help maintain structural reliability throughout the service life and reduce maintenance burdens. A systematic study was conducted to investigate the effects of CTAB and PEG surfactants on the characterization and morphology of ZnO NPs, as well as their anti-corrosion properties when incorporated with PLA.

2. Materials and methods

2.1. Materials

AA2024-T3 (Al 93.20%, Cu 4.35%, Mg 1.32%, Mn 0.57%, Fe 0.29%, Cr 0.18%, Si 0.09%). Resin Polylactic Acid (PLA) was sourced from Shenzhen Esun Industrial with an average molecular weight ≈ 100,000 $g \cdot mol^{-1}$. Zinc Acetate dihidrate ($Zn(CH_3COO)_2 \cdot 2H_2O$), natrium hydroxide (NaOH), cethyltrimetyl ammonium bromide/CTAB (Merck), polyethylene glycol/PEG (Alpha Chemical), and hydrochloric acid (HCl) 1 M were obtained from Sigma Aldrich of AR grade.

2.2. Methods

This study involves the synthesis of ZnO NPs, the preparation of PLA based nanocomposites, the application of coatings on AA2024-T3, and the evaluation of corrosion resistance. ZnO NPs were synthesized via a precipitation method using zinc acetate dihydrate as the precursor in ethanol, with the addition of NaOH to induce precipitation, and with CTAB and PEG surfactants to improve particle characteristics and prevent ZnO nanoparticle agglomeration, yielding ZnO, ZnO/CTAB, and ZnO/PEG. The ZnO NPs were then dispersed into a PLA solution to obtain a homogeneous nanocomposite solution through magnetic stirring and ultrasonication. AA2024-T3 substrates were prepared by mechanical polishing and cleaning, followed by coating using the dip

coating method and thermal drying to enhance coating adhesion. The corrosion resistance of the coatings was evaluated by electrochemical testing using Tafel polarization and EIS methods in a three-electrode system. Immersion tests were conducted on AA2024-T3 samples coated with PLA/ZnO nanocomposites in 1 M HCl solution for 5 days to examine the surface morphology of the alloy. Corrosion inhibition efficiency was determined based on the reduction in corrosion current density and the increase in charge transfer resistance, while FTIR and SEM analyses were performed to assess chemical stability and surface morphology changes before and after corrosion testing.

2.2.1. Synthesis of ZnO NPs

ZnO NPs were prepared by a precipitation route adapted from earlier work [15,35] with slight modifications (Fig. 1a). 2.726 g of zinc acetate dihydrate [$Zn(CH_3COO)_2{\cdot}2H_2O$] was dissolved in 30 mL of absolute ethanol, followed by magnetic stirring at 800 rpm for 30 min at 60 °C. For the surfactant assisted samples, the precursor solution was supplemented with 30 mL of 0.01 M CTAB or 30 mL of 0.01 M PEG. Next, 10 mL of 3 M NaOH was introduced dropwise into each mixture to induce the formation of a white precipitate. The resulting solid was recovered by vacuum filtration using a Büchner funnel, rinsed with deionized water until the pH approached neutrality (~7), and dried at 60 °C for 6 h. The dried powders were then ground to ensure homogeneity and calcined at 300 °C for 2 h in separate vessels, producing three nanoparticle powders: ZnO, ZnO/CTAB, and ZnO/PEG.

2.2.2. Characterization techniques

UV–Visible absorption spectra of the nanoparticles ZnO, ZnO/CTAB and ZnO/PEG were recorded using a Shimadzu UV-1601 spectrophotometer over the wavelength range of 200–800 nm, with ethanol used as the blank. FTIR spectra were acquired using an IRSpirit Shimadzu instrument equipped with an attenuated total reflectance (ATR) accessory in the wavenumber range of 4000–400 cm^{-1}. The crystal structure was examined by X-ray diffraction (XRD) using a PANalytical X'Pert^3 Powder diffractometer in the 2θ range of 20°–80°. The particle size and surface morphology were analyzed by scanning electron microscopy (SEM) using a Quanta FEG 650 system, while elemental composition and distribution were determined by energy dispersive X-ray spectroscopy (EDX) coupled with the SEM.

Nitrogen adsorption–desorption isotherms were measured at 77 K using a Micromeritics NOVA 4LX surface area and porosity analyzer after degassing the samples at 473 K for 12 h. The pore size distribution was calculated from the adsorption branch of the isotherm using the Barrett–Joyner–Halenda (BJH) method.

2.2.3. Preparation of PLA based nanocomposite

Nanocomposite coating solutions were prepared by dispersing 0.05 g of ZnO NPs (with and without surfactant) into 100 mL of a PLA solution, followed by magnetic stirring at 50 °C until a uniform mixture was obtained (Fig. 1b). The suspension was then ultrasonicated for 30 min to ensure homogeneous nanoparticle dispersion within the PLA matrix [22].

2.2.4. Coating AA2024-T3

AA2024-T3 substrates (1 cm × 2 cm × 0.2 cm) were mechanically polished using SiC abrasive papers (400–2000 grit), ultrasonically cleaned in ethanol and distilled water for 10 min each, and air dried at room temperature. Dip coating was applied in this work: the pretreated substrates were slowly immersed in the nanocomposite solution and held for 30 min to allow uniform film formation. After withdrawal, the coated samples were air dried and subsequently thermally cured at 60 °C for 2 h to remove residual solvent and enhance coating adhesion [22].

2.2.5. Corrosion testing

Prior to the Tafel polarization measurements, the Autolab PGSTAT204 was validated using the manufacturer's built in diagnostic procedure to ensure accurate operation and instrument integrity. Electrochemical tests were performed in a standard three electrode configuration, where AA2024-T3 served as the working electrode, Ag/AgCl (3 M KCl) as the reference electrode, and a platinum electrode as the counter electrode. For reproducibility assessment, each coating system was evaluated using independent AA2024-T3. The reported electrochemical metrics, including corrosion current density (i_{corr}), charge transfer resistance (R_{ct}), and inhibition efficiency (%IE), are expressed

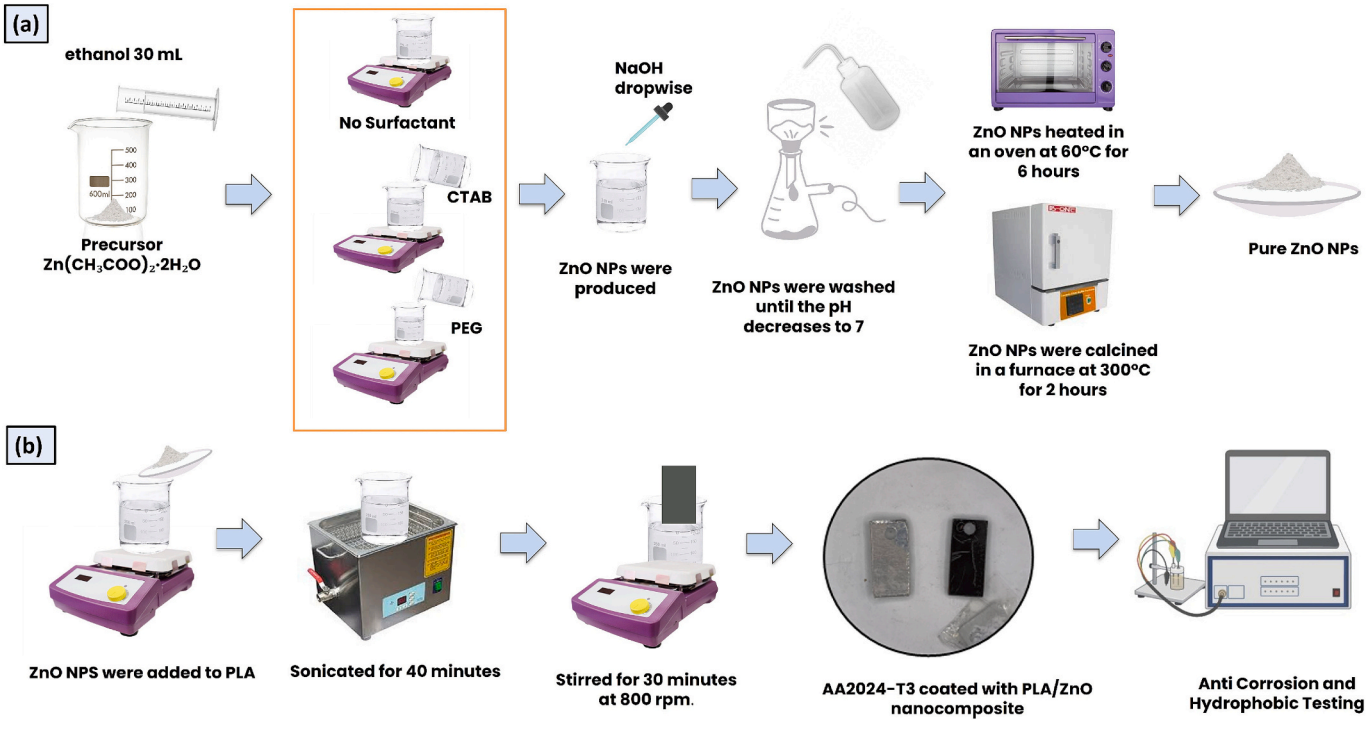

Fig. 1. Schematic illustration of ZnO NPs synthesis (a), and Preparation of ZnO/PLA nanocomposite and coating deposition on AA2024-T3 (b).

as mean values ± standard deviations. The AA2024-T3 specimens subjected to anticorrosion testing were subsequently immersed in 1 M HCl for 5 days to evaluate their corrosion resistance [36]. The coated AA2024-T3 samples before and after HCl immersion were then characterized by FTIR and SEM to assess chemical stability and changes in the alloy surface morphology.

Potentiodynamic Polarization (PP) measurements were performed at a scan rate of 1 m*V*/s, covering a potential range of ±0.1 V relative to E_{corr}. This specific scan rate was selected based on our previous study [22], as it consistently produces stable polarization curves ideal for detailed corrosion analysis. The scan rate of 1 mV/s was chosen to ensure a near steady state condition, reduce capacitive current interference, and allow precise determination of electrochemical parameters such as corrosion potential and current density. This value is commonly used in studies involving PLA-or ZnO based composites in acidic media.

Calculation of inhibition efficiency based on the PP test by Eq. (1) [14,37]:

$$IE\% = \frac{i_{corr} - i_{corr(i)}}{i_{corr}} \times 100 \quad (1)$$

where $i_{(corr)}$ and $i_{(corr(i))}$ denote the corrosion current densities measured for the blank and coated samples (PLA, PLA/ZnO, PLA/ZnO/CTAB, and PLA/ZnO/PEG) nanocomposite inhibitors.

EIS measurements were carried out at OCP with a 10 mV AC excitation over the frequency range of 10^5–0.01 Hz, and the corrosion inhibition efficiency was evaluated using Eq. (2) [22,38]:

$$IE\% = \frac{R_p - R_{p(i)}}{R_p} \times 100 \quad (2)$$

where R_p and $R_p(i)$ represent polarization resistance values obtained in the blank and coated with PLA, PLA/ZnO, PLA/ZnO/CTAB and PLA/ZnO/PEG nanocomposite inhibitors, respectively.

2.2.6. Monte Carlo simulation

Monte Carlo simulations were conducted using the Adsorption Locator module in BIOVIA Materials Studio 2020 to identify the most stable adsorption configurations of the PLA/ZnO system on the Al (1 1 1) surface. The Al (1 1 1) slab model was constructed with periodic boundary conditions and a 20 Å vacuum layer to avoid interlayer interactions. The PLA polymer and ZnO nanoparticles were modeled based on their structures and optimized using the COMPASS II force field. To simulate an acidic environment, chloride ions (Cl^-) and water molecules were included to evaluate competitive adsorption behavior. The adsorption energy (E_{ads}) was calculated using Eq. (3).

$$E_{ads} = E_{total} - (E_{surface} + E_{adsorbate}) \quad (3)$$

where E_{total} represents the total system energy, $E_{surface}$ corresponds to the energy of the clean Al (1 1 1) surface, and $E_{adsorbate}$ denotes the energy of the isolated PLA/ZnO species. A more negative E_{ads} reflects stronger adsorption and a higher potential for corrosion inhibition.

The Monte Carlo simulation explored various molecular orientations and conformations to determine the most stable adsorption configuration. The results were further supported by analyzing interaction sites, adsorption distribution, and molecular alignment, providing a theoretical basis for the observed corrosion inhibition behavior.

3. Results and discussion

3.1. Modification and characterization of ZnO NPs

This stage was carried out by synthesizing ZnO NPs with and without surfactants, followed by characterization using UV–Vis spectroscopy, FTIR, and XRD, as well as morphological analysis using SEM. Fig. 2 presents a comprehensive characterization of ZnO NPs synthesized with and without CTAB and PEG (surfactants) modification. ZnO NPs typically exhibit a relatively broad absorption band with an absorption onset in the 360–380 nm range [39]. In this study, ZnO NPs synthesized with and without surfactant addition were characterized by UV–Vis spectroscopy. The absorption spectra display a characteristic peak at 366 nm for pristine ZnO, whereas ZnO/CTAB and ZnO/PEG show peaks at 376 nm and 373 nm, respectively. The presence of these peaks confirms the phase purity of the prepared ZnO NPs (Fig. 2a). The red-shift observed for the surfactant modified ZnO is attributed to altered nucleation and crystal growth kinetics, which can promote an increase in crystallite size [40,41]. CTAB and PEG act as templating agents during mesopore formation, leading to a tendency toward larger particle sizes and a shift of the absorption feature toward longer wavelengths, while remaining within the typical absorption region of ZnO [42–44].

FTIR analysis was performed to identify the vibrational modes of functional groups in the synthesized NPs over the wavenumber range of 4500–500 cm^{-1} at room temperature. A strong and sharp absorption band at 531 cm^{-1}, assigned to Zn—O stretching vibration, confirms the formation of ZnO NPs (Fig. 2b). The addition of surfactants does not induce any significant changes in the FTIR spectra, indicating that no strong new chemical bonds are formed between CTAB or PEG and the ZnO lattice [35,45,46].

The X-ray diffraction (XRD) patterns of ZnO NPs, both with and without surfactants, exhibit three major diffraction peaks at 2θ = 31.74°, 34.42°, and 36.21°, corresponding to the (1 0 0), (0 0 2), and (1 0 1) planes of the hexagonal wurtzite ZnO structure (Fig. 2c). The narrow, high intensity peaks indicate fine grain size and high crystallinity. The absence of additional diffraction peaks in the surfactant modified samples confirms that the hexagonal wurtzite crystal structure is preserved after the incorporation of CTAB and PEG [21,47].

SEM was used to observe the morphology, shape, and surface texture of ZnO NPs. Fig. 3 provides a comparative overview of the morphology and elemental composition of three nanoparticle systems, pristine ZnO,

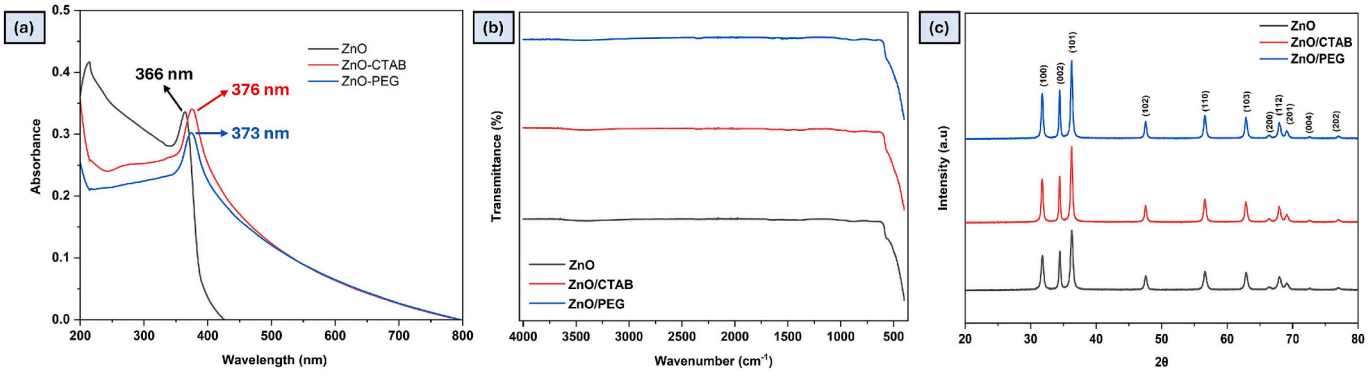

Fig. 2. (a) UV–Vis spectra, (b) FTIR spectra, and (c) XRD patterns for ZnO, ZnO/CTAB, and ZnO/PEG.

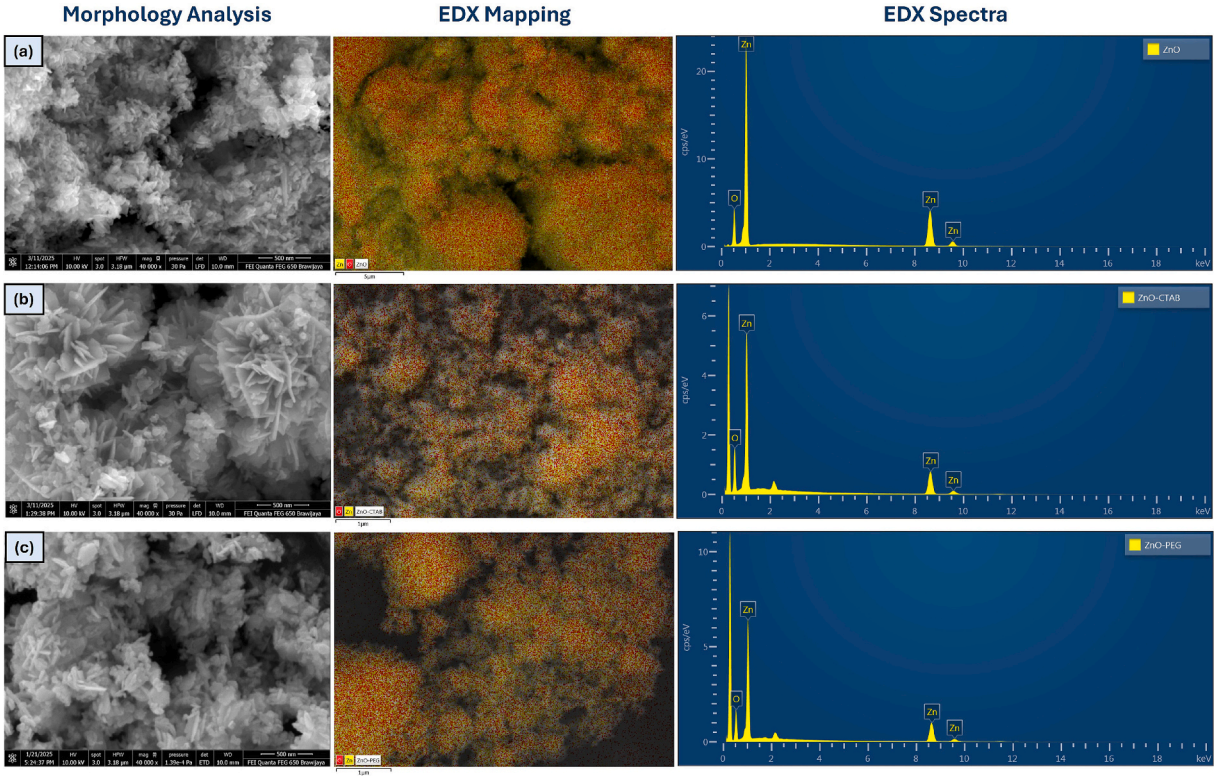

Fig. 3. SEM micrographs and EDX analysis (elemental mapping and spectra) of (a) ZnO, (b) ZnO/CTAB, and (c) ZnO/PEG NPs.

ZnO modified with CTAB (ZnO/CTAB), and ZnO modified with PEG (ZnO/PEG), as characterized by scanning electron microscopy (SEM) and energy dispersive X-ray spectroscopy (EDX). For each sample, the left panels present SEM micrographs to evaluate particle shape, surface texture, and the extent of agglomeration, the middle panels display EDX elemental maps to assess the spatial distribution and uniformity of the constituent elements, and the right panels show the corresponding EDX spectra to qualitatively confirm the dominant elemental signatures. This integrated presentation is intended to elucidate how the incorporation of CTAB as a surfactant and PEG as a polymeric modifier/structure directing agent influences nanoparticle assembly and surface architecture while maintaining the characteristic ZnO elemental framework across the investigated materials [48,49].

The SEM image of nanoparticle ZnO (Fig. 3a) reveals fine particles forming pronounced agglomerated clusters with a heterogeneous surface texture and visible inter aggregate voids, indicating a strong tendency toward particle aggregation during synthesis and drying. The incorporation of surfactants such as CTAB (Fig. 3b) during ZnO synthesis leads to the formation of nanoflake structures because these surfactants selectively adsorb onto particular crystal facets, suppress growth in specific directions, and favor anisotropic crystal growth [50,51]. In contrast, ZnO/PEG (Fig. 3c) exhibits a more distinct morphological evolution, showing hierarchical, flower rosette like architectures composed of assembled nanoflake like subunits, suggesting that PEG acts as a structure directing and growth controlling agent by modulating nucleation and crystal growth pathways [34,52].

The addition of surfactants in nanoparticle synthesis causes changes in elemental distribution, as shown in Table 1. For example, zinc (Zn) was detected at 59.22% in the ZnO/CTAB sample and 69.16% in the ZnO/PEG sample, which are lower compared to the ZnO sample at 77.66%. This is presumably because the addition of surfactants plays a role in preventing particle agglomeration, causing the nanoparticles to be more evenly dispersed. As the particles are dispersed rather than aggregated, the Zn elemental distribution at the points analyzed by EDS decreases in the ZnO/CTAB and ZnO/PEG samples.

Table 1
EDX analysis nanoparticles ZnO.

Sample NPs	Zinc (Zn)		Oxygen (O)	
	Weight (%)	Atomic (%)	Weight (%)	Atomic (%)
ZnO	77.66	45.97	22.34	54.03
ZnO/CTAB	59.22	26.22	40.78	73.78
ZnO/PEG	69.16	33.94	24.49	49.11

In addition, surfactants also cause pores on the surface of nanoparticles, which lead to crystal defects. Crystal defects are phenomena in which the arrangement of particles within a crystal structure deviates from the periodic repetition of spatial lattice laws, resulting in irregularities in the crystal structure [53–55]. In nanoparticles, which are 0-dimensional materials, crystal defects that may arise are point defects. Point defects include vacancies (an atom missing from its normal lattice position, leaving an empty space), interstitial atoms (additional atoms entering the interstitial space), substitutional atoms (a foreign atom replacing the main atom), Frenkel defects (an atom leaving its normal lattice position and occupying an interstitial position), and Schottky defects (a pair of oppositely charged ions missing from the lattice, creating an empty space) [56]. The presence of certain additives, such as surfactants, can adsorb at the crystal interface, leading to crystal defects, thus affecting the elemental distribution observed through EDS characterization. The carbon atoms (C) present in the ZnO/PEG sample are likely due to impurities during the synthesis procedure [57].

Nitrogen adsorption–desorption analysis using the Brunauer–Emmett–Teller (BET) method was performed to evaluate the surface textural characteristics of ZnO nanoparticles synthesized using CTAB and PEG as templating agents. The resulting hysteresis isotherms are presented in Fig. 4, while the corresponding specific surface area and pore size data are summarized in Table 2.

BET analysis revealed that both ZnO/CTAB and ZnO/PEG exhibit type IV nitrogen adsorption–desorption isotherms with a distinct

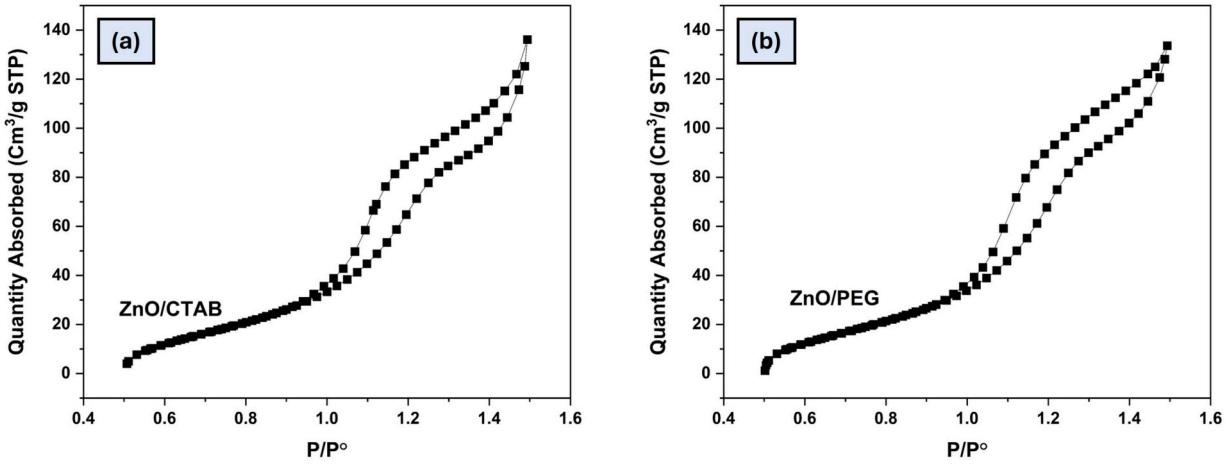

Fig. 4. Nitrogen adsorption−desorption isotherms of the ZnO/CTAB (a) and ZnO/PEG NPs (b).

Table 2
Specific surface area and pore size of ZnO/CTAB, ZnO/PEG NPs.

Sample NPs	Specific surface area(m^2/g)	Average pore size (nm)
ZnO/CTAB	10.63	11.07
ZnO/PEG	3.49	34.33

hysteresis loop, confirming the mesoporous nature of the materials. As summarized in Table 2, ZnO/CTAB shows a higher specific surface area (10.63 m^2/g) with a smaller average pore size of 11.07 nm, indicating the formation of finer and more uniformly distributed mesopores. In contrast, ZnO/PEG presents a lower surface area (3.49 m^2/g) with a larger average pore size (34.33 nm), suggesting a more open mesoporous structure. These results highlight the critical role of templating agents in controlling pore size distribution and surface area of ZnO nanoparticles, which directly affects their functional performance. ZnO pores with widths ranging from 2 to 50 nm confirm the mesoporous nature of the samples [58,59].

3.2. Characterization of nanocomposites

In the subsequent stage, the synthesized nanocomposite was characterized using UV–Vis spectroscopy and FTIR analysis. The results of these characterizations are presented in Fig. 5. The UV–Vis spectra (Fig. 5a) are used to compare the light matter interaction of PLA based coatings after ZnO addition and CTAB assisted modification, whereas the FTIR spectra (Fig. 5b) are provided to verify the preservation of the PLA backbone and to assess whether introducing ZnO and CTAB alters the dominant functional groups of the coating matrix. All of these results offer complementary evidence linking coating formulation to optical uniformity and chemical stability.

The UV–Vis spectra exhibit the same absorption peak at 376 nm for all samples (Fig. 5a), indicating that the position of the absorption edge remains essentially unchanged. The absorbance intensity varies among the formulations, with PLA/ZnO/CTAB showing the lowest value (~0.5). This variation is mainly influenced by optical and morphological factors, such as reduced light scattering due to improved nanoparticle dispersion and a possible decrease in the effective ZnO fraction. In addition, the presence of a CTAB layer on the ZnO surface can passivate active sites, thereby lowering the absorption intensity without shifting the peak position [60]. The UV shielding efficiency of PLA/ZnO/CTAB nanocomposites is lower than that of systems without surfactant or those modified with PEG. It is important to note that UV shielding is not the primary factor governing corrosion protection in this system. The anti-corrosion performance is predominantly controlled by barrier-related properties, including nanoparticle dispersion, mesoporosity, hydrophobicity, and the resulting tortuous pathways that limit the diffusion of aggressive species such as Cl^- and water. While UV shielding may contribute to reducing long-term photodegradation of the polymer matrix, its effect becomes significant only under UV exposure conditions. Since the corrosion evaluation in this study was conducted in the

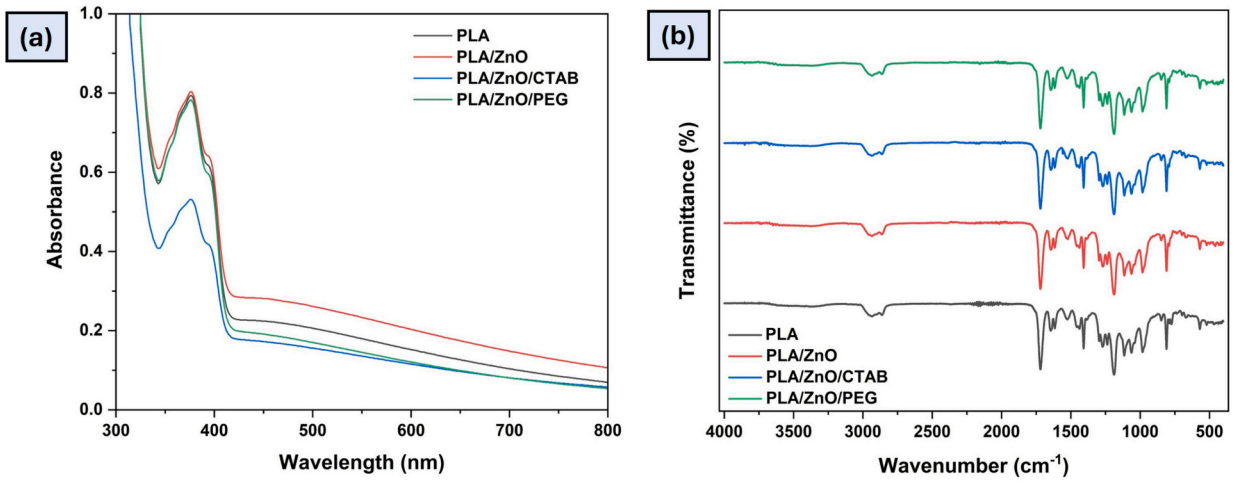

Fig. 5. UV–Vis absorbance spectra (a) and FTIR spectra (b) of the PLA, PLA/ZnO, PLA/ZnO/CTAB and PLA/ZnO/PEG nanocomposites.

absence of UV irradiation, the lower UV shielding efficiency of PLA/ZnO/CTAB does not directly correlate with its corrosion resistance performance.

FTIR spectra of all formulations are broadly similar and dominated by the characteristic vibrational bands of PLA, including the ester carbonyl stretching band (C═O, typically near ~1750 cm^{-1}), C—O—C/C—O stretching bands (commonly in the ~1180–1080 cm^{-1} region), and C—H stretching bands (typically ~3000–2850 cm^{-1}) (Fig. 5b). After ZnO incorporation, with or without CTAB/PEG, no prominent new bands or systematic large shifts are observed, suggesting that the nanocomposite formation is governed mainly by physical incorporation and weak interfacial interactions (e.g., dipolar interactions and limited hydrogen bonding) rather than the formation of new dominant chemical functionalities in the PLA backbone [44].

3.3. Potentiodynamic polarization, electrochemical impedance spectroscopy and wettability analysis

The corrosion behavior of AA2024-T3 coated with PLA based nanocomposites was evaluated using tafel and nyquist measurements, as shown in the Tafel plots (Fig. 6). The tafel curves of blank AA2024-T3 and coated samples are presented in Fig. 6a and Table 3. AA2024-T3 blank exhibits the highest corrosion current density (i_{corr}), indicating severe electrochemical activity in the corrosive medium. This behavior is attributed to the direct exposure of the AA2024-T3 surface to aggressive ions.

The PLA coated sample shows a noticeable reduction in i_{corr} compared to the blank substrate, confirming the role of PLA as a physical barrier that restricts the penetration of corrosive species. Further improvement is observed after incorporating ZnO NPs into the PLA matrix, where the PLA/ZnO coating exhibits a lower corrosion current density. This enhancement is associated with the pore filling effect and increased tortuosity of diffusion pathways induced by the presence of ZnO nanofillers [61,62].

The best corrosion protection performance is achieved by the PLA/ZnO coatings modified with CTAB and PEG surfactants. These coatings display the lowest i_{corr} values along with a positive shift of the corrosion potential E_{corr} suggesting a significant suppression of both anodic metal dissolution and cathodic reactions. The superior performance is mainly attributed to improved nanoparticle dispersion and reduced agglomeration, resulting in a more compact and homogeneous coating structure that effectively impedes charge transfer at the metal–electrolyte interface [22,32,63].

The Nyquist plots obtained from EIS measurements are shown in Fig. 6b and Table 4. The bare AA2024-T3 exhibits the smallest semicircle diameter, reflecting a low charge transfer resistance (R_{ct}) and a high corrosion rate. All coated samples present significantly larger semicircles, indicating enhanced corrosion resistance. Electrochemical impedance spectroscopy (EIS) results demonstrate a progressive

Table 3
The corrosion parameters were determined by extrapolating the tafel polarization curves of AA2024-T3.

Sample	E_{corr} (V)	i_{corr} (A/cm^2)	Corrosion rate (mm/year)	Inhibition Efficiency (%)
AA2024-T3 Blank	−8.22 ± 0.1 × 10^{-1}	6.89 ± 0.11 × 10^{-3}	188.08	0.00
AA2024-T3 + PLA	−8.14 ± 0.12 × 10^{-1}	5.24 ± 0.1 × 10^{-3}	60.75	67.70
AA2024-T3 + PLA/ZnO	−8.02 ± 0.11 × 10^{-1}	2.98 ± 0.15 × 10^{-4}	3.46	98.16
AA2024-T3 + PLA/ZnO/CTAB	−7.89 ± 0.13 × 10^{-1}	1.03 ± 0.12 × 10^{-4}	1.20	99.36
AA2024-T3 + PLA/ZnO/PEG	−7.92 ± 0.12 × 10^{-1}	1.12 ± 0.13 × 10^{-4}	1.30	99.31

Table 4
The corrosion parameters were determined by extrapolating the EIS of AA2024-T3.

Sample	Rs ($\Omega \cdot cm^2$)	CPE (T)	CPE-P	Rp ($\Omega \cdot cm^2$)	IE_{EIS} (%)
AA2024-T3 Blank	1.15 ± 0.01	5.06 ± 0.12 × 10^{-5}	0.83 ± 0.02	19.54 ± 0.1	0.0
AA2024-T3 + PLA	2.43 ± 0.02	3.42 ± 0.11 × 10^{-5}	0.92 ± 0.01	75.68 ± 0.12	74.2
AA2024-T3 + PLA/ZnO	2.03 ± 0.02	8.74 ± 0.13 × 10^{-6}	0.95 ± 0.02	98.85 ± 0.11	80.2
AA2024-T3 + PLA/ZnO/CTAB	2.08 ± 0.02	6.33 ± 0.12 × 10^{-6}	0.98 ± 0.03	155.77 ± 0.16	87.4
AA2024-T3 + PLA/ZnO/PEG	2.05 ± 0.01	6.51 ± 0.15 × 10^{-6}	0.96 ± 0.01	132.51 ± 0.17	85.3

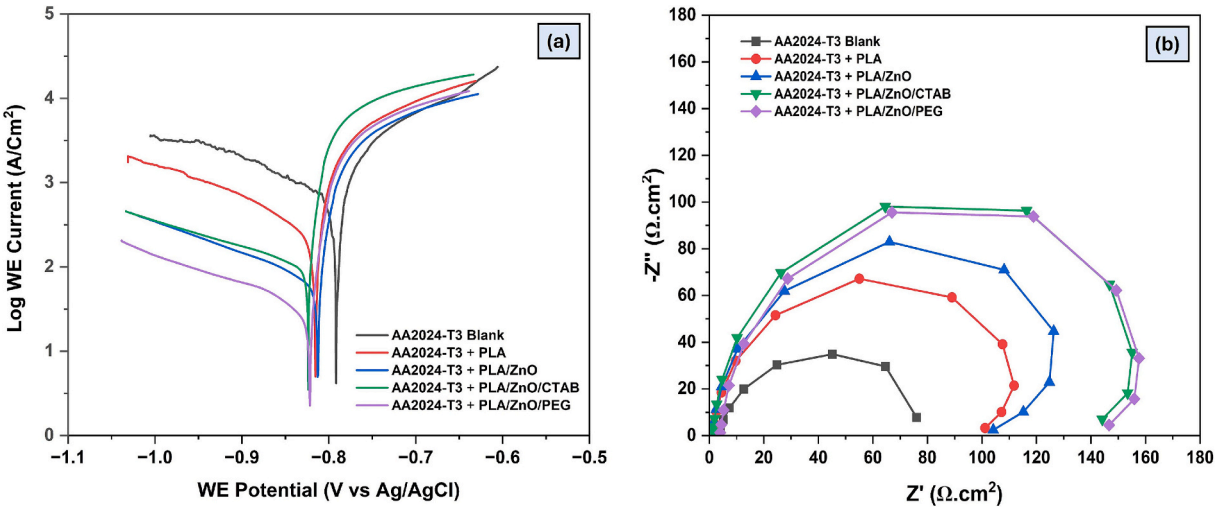

Fig. 6. (a) Potentiodynamic polarization curves and (b) Nyquist plots of AA2024-T3 substrate: uncoated (blank) and coated with PLA, PLA/ZnO, PLA/ZnO/CTAB, and PLA/ZnO/PEG.

enhancement in the corrosion resistance of AA2024-T3 after the incorporation of ZnO nanoparticles, particularly those synthesized using surfactant templates. The uncoated substrate exhibited the lowest polarization resistance (Rp) of 19.54 $\Omega \cdot cm^2$, confirming its high susceptibility to corrosion. The application of neat PLA increased Rp to 75.68 $\Omega \cdot cm^2$ with an inhibition efficiency of 74.2%, reflecting the intrinsic barrier effect of the polymer matrix. The addition of ZnO nanoparticles into the PLA matrix further improved the electrochemical performance, as indicated by the increase of Rp to 98.85 $\Omega \cdot cm^2$ and a decrease in CPE-T to the order of 10^{-6} F. This reduction in capacitance suggests lower water uptake and restricted electrolyte penetration due to the filler effect of ZnO, which increases the tortuosity of ion diffusion pathways.

A more pronounced improvement was observed for PLA/ZnO/CTAB and PLA/ZnO/PEG coatings, which exhibited Rp values of 155.77 and 132.51 $\Omega \cdot cm^2$ with inhibition efficiencies of 87.4% and 85.3%, respectively. These enhancements correlate strongly with the BET results, where surfactant-templated ZnO displayed higher specific surface area and mesoporous characteristics compared to non-modified ZnO. The presence of mesopores (20–33 nm) promotes better interfacial interaction between ZnO and the PLA matrix, leading to improved nanoparticle dispersion and reduced agglomeration [14,64]. It is important to note that inhibition efficiencies derived from Tafel polarization are generally higher than those obtained from EIS due to the different evaluation principles. Tafel reflects instantaneous corrosion kinetics, whereas EIS is more sensitive to coating defects, porosity, and long-term barrier properties, which may result in relatively lower apparent efficiencies [36].

Additionally, mesoporosity (pore size can be seen in Table 1) plays a crucial role in enhancing anticorrosion performance by influencing the barrier properties and transport behavior of corrosive species within protective coatings. Mesoporous structures, characterized by pore sizes in the range of 2–50 nm, can promote a more uniform dispersion of functional fillers and increase interfacial adhesion between the coating and the substrate. Mesopores can act as controlled pathways that trap or delay the diffusion of aggressive ions, such as Cl^- and H_2O, thereby reducing their direct interaction with the metal surface. The presence of well distributed mesopores contributes to improved coating integrity, enhanced barrier efficiency, and prolonged corrosion protection [65–67].

To evaluate the wettability of the AA2024-T3 before and after surface modification, water contact angle measurements were performed, as shown in Fig. 7. The droplet profiles and fitted contours illustrate how the coatings alter the solid liquid interaction, enabling direct visual comparison of the wettability/hydrophobicity evolution from the bare substrate to the hybrid coating systems.

The water contact angle observations indicate a clear wettability shift of AA2024-T3 from hydrophilic to increasingly hydrophobic after coating. The blank surface shows pronounced droplet spreading, consistent with high surface energy associated with polar Al oxide/hydroxide species, whereas PLA coating produces a more spherical droplet with a reduced contact footprint due to formation of an organic barrier that masks polar sites and lowers surface energy. Incorporation of ZnO into PLA further stabilizes the droplet shape, which is attributable to micro/nano topography modification and increased effective roughness that amplifies non wetting behavior when combined with the intrinsically lower surface energy of the polymer matrix [68,69]. The PLA/ZnO/CTAB coating yields the most stable, most spherical droplet profile, reflecting the lowest wettability, plausibly because CTAB improves ZnO dispersion and coating uniformity while promoting a more effective micro/nano texture and reducing the effective surface energy at the outer interface [70–72].

3.4. Post immersion surface characterization of AA2024-T3

The surface morphology and chemical characteristics of AA2024-T3 after immersion for 5 days in 1 M HCl, analyzed using SEM, EDX mapping, and EDX spectra, show reduced corrosion products and improved surface coverage for the hybrid coatings compared with the uncoated alloy, as summarized in Fig. 8. The quantitative elemental compositions derived from EDX analysis are summarized in Table 5.

The blank AA2024-T3 surface (Fig. 8a) exhibits a highly heterogeneous and rough morphology characterized by irregular features and micro scale defects. This morphology is typical of AA2024-T3 and is associated with the presence of native oxide layers and intermetallic phases. The EDX spectrum and elemental mapping confirm that the surface is dominated by aluminum and oxygen, with oxygen accounting for 38.94 wt% (58.31 at.%), indicating the formation of a naturally occurring aluminum oxide layer. Minor zinc signals are detected, which are attributed to trace alloying constituents rather than surface modification. Following the deposition of the PLA/ZnO coating (Fig. 8b and c), significant changes in both surface morphology and elemental composition are observed. The coated surfaces show partial coverage by

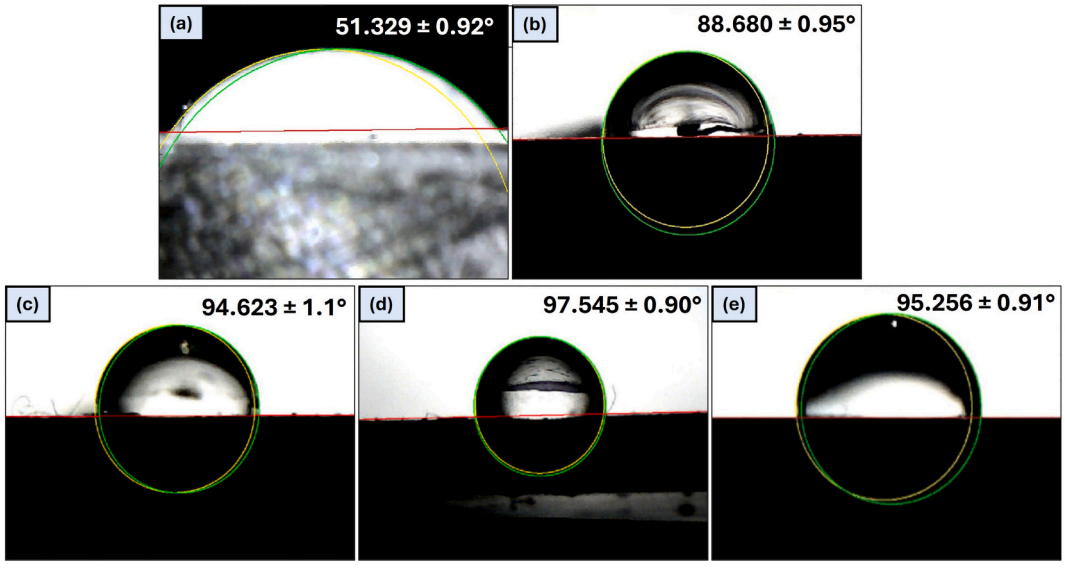

Fig. 7. Water contact angle images showing the wettability of AA2024-T3 surfaces: (a) AA2024-T3 blank, (b) AA2024-T3 + PLA, (c) AA2024-T3 + PLA/ZnO, and (d) AA2024-T3 + PLA/ZnO/CTAB (e) AA2024-T3 + PLA/ZnO/PEG.

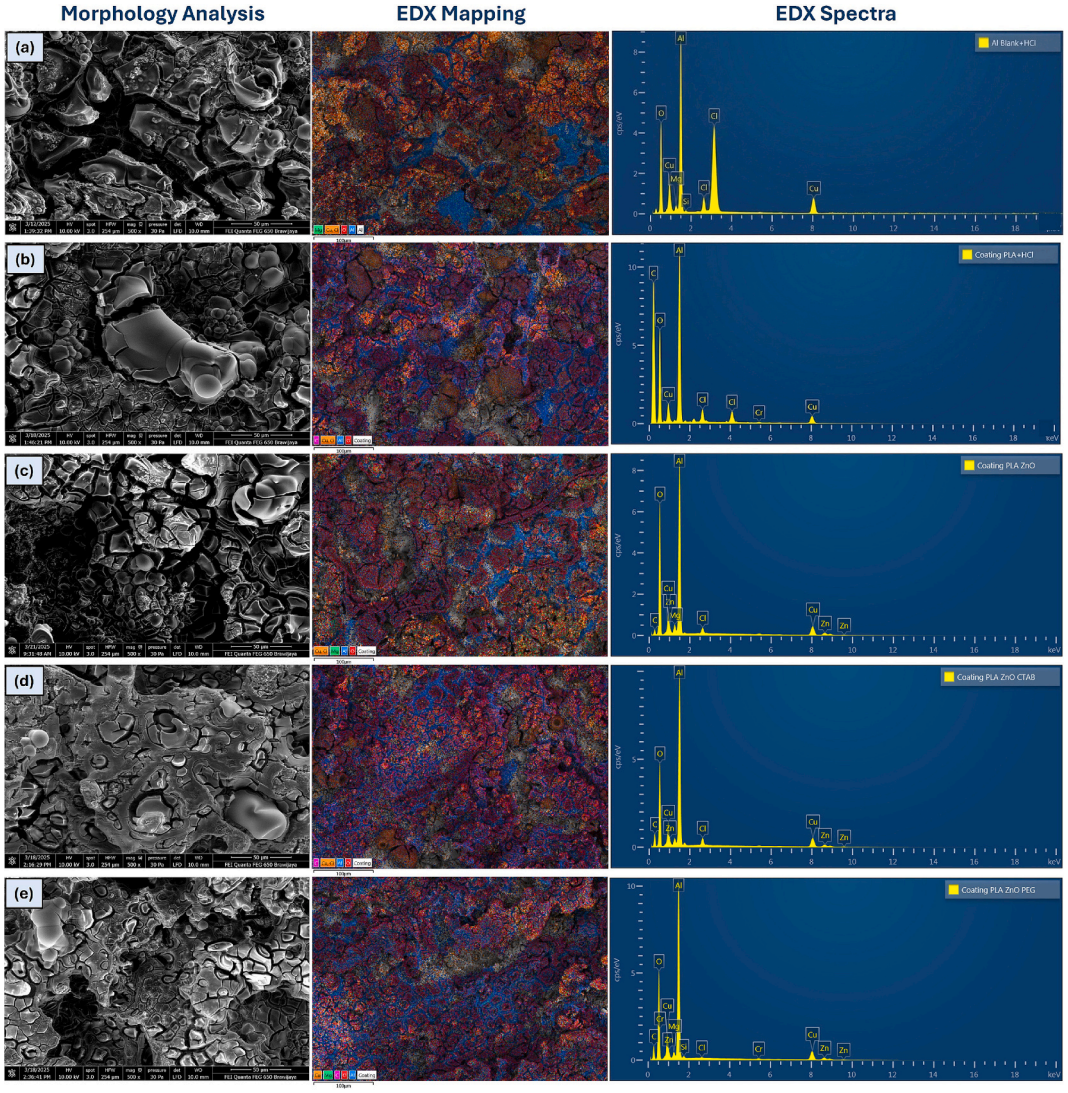

Fig. 8. SEM micrographs (left), EDX elemental maps (middle), and EDX spectra (right) of AA2024-T3 surfaces after 5 days of immersion in HCl: (a) AA2024-T3 blank, (b) AA2024-T3 + PLA, (c) AA2024-T3 + PLA/ZnO, (d) AA2024-T3 + PLA/ZnO/CTAB, and (e) AA2024-T3 + PLA/ZnO/PEG.

Table 5
EDX analysis AA2024-T3 blank and coated nanocomposites.

Sample	Oxygen (O)		Aluminum (Al)		Zinc (Zn)		Carbon (C)	
	Weight (%)	Atomic (%)	Weight (%)	Atomic (%)	Weight (%)	Atomic (%)	Weight (%)	Atomic (%)
AA2024T3 Blank	39.75	59.23	34.12	28.15	–	–	–	–
AA2024-T3 + PLA	46.12	55.25	28.27	20.86	–	–	25.80	23.36
AA2024-T3 + PLA/ZnO	49.11	60.97	26.88	19.78	3.35	1.02	8.04	13.30
AA2024-T3 + PLA/ZnO/CTAB	40.23	47.14	25.67	17.83	2.94	0.84	19.51	30.45
AA2024-T3 + PLA/ZnO/PEG	41.00	47.50	24.87	17.09	2.90	0.82	19.90	30.72

a polymeric layer, accompanied by embedded nanostructured features attributed to ZnO NPs [73].

Quantitative EDX results reveal a marked increase in carbon content, reaching up to 12.80 wt% (20.63 at.%), which confirms the successful deposition of the PLA matrix on the AA2024-T3 substrate. Simultaneously, the atomic fraction of AA2024-T3 decreases compared to the blank sample, indicating effective surface coverage by the polymer–nanoparticle coating [26]. The presence of zinc, with contents ranging from 2.48 to 3.35 wt%, further confirms the incorporation of ZnO NPs within the coating layer. Localized agglomeration and surface heterogeneities are still evident, suggesting limited nanoparticle dispersion in the absence of surfactant modification [44,74]. A more pronounced improvement in surface uniformity is observed for the surfactant modified coatings (PLA/ZnO/CTAB and PLA/ZnO/PEG), as shown in Fig. 8d and e. These samples exhibit smoother and more continuous morphologies with fewer visible defects and agglomerates. EDX mapping demonstrates a more homogeneous spatial distribution of zinc and carbon across the surface, indicating enhanced dispersion of ZnO NPs within the PLA matrix. The carbon content increases significantly to 19.51 wt% (30.45 at.%) and 19.90 wt% (30.72 at.%) for the CTAB and PEG modified coatings, respectively, while the aluminum content further decreases. These results suggest a higher fraction of organic

material at the surface and the formation of a thicker and more compact coating layer.

The mapping element images as shown in Fig. 9 reveal a clear difference in the dispersion state of ZnO nanoparticles within the PLA matrix. The PLA ZnO coating without surfactant exhibits noticeable particle agglomeration, indicating limited interfacial compatibility. Meanwhile, the PLA/ZnO/CTAB and PLA/ZnO/PEG systems present a more homogeneous and uniform distribution of ZnO nanoparticles, with a significant reduction in agglomerate size and improved surface continuity. The improved elemental homogeneity observed in Fig. 9 is attributed to the ability of CTAB and PEG to reduce nanoparticle agglomeration and promote stronger interfacial interactions between ZnO, the PLA matrix, and the AA2024-T3 substrate [21,50]. This enhanced dispersion arises from the role of surfactants in minimizing interparticle interactions and improving compatibility within the composite system. Such microstructural refinement leads to the formation of a more compact and effective barrier structure by minimizing defect pathways and restricting the diffusion of aggressive species toward the metal surface [37]. This structural improvement contributes to the enhanced corrosion resistance observed in the electrochemical measurements, which is consistent with the superior corrosion protection performance of the surfactant modified coatings reported in subsequent analyses [68], and provides direct structural evidence supporting the proposed dispersion driven anticorrosion mechanism.

3.5. Monte Carlo (MC) simulation analysis

Table 6 and Fig. 10 present the adsorption energy parameters obtained from Monte Carlo (MC) simulations for PLA and PLA/ZnO systems, providing insight into their interfacial interactions and corrosion inhibition performance. The PLA/ZnO system exhibits a significantly more negative adsorption energy (-4.4×10^6 kcal·mol^{-1}) compared to pristine PLA (-4.56×10^3 kcal·mol^{-1}), indicating a substantially stronger and more stable adsorption onto the metal surface. This trend is consistent with the deformation energy values, where PLA/ZnO also shows a much higher magnitude (-4.4×10^6 kcal·mol^{-1}) than PLA (-4.11×10^3 kcal·mol^{-1}), suggesting enhanced structural adaptation during adsorption. In addition, the rigid adsorption energy of PLA/ZnO (-626.88 kcal·mol^{-1}) is more negative than that of PLA (-461.40 kcal·mol^{-1}), confirming stronger intrinsic interactions even without structural relaxation. The inhibitor efficiency parameter (dE_{ad}/dN_i) also demonstrates a markedly higher value for PLA/ZnO (-4.39×10^6 kcal·mol^{-1}) compared to PLA (-4.47×10^4 kcal·mol^{-1}), indicating superior inhibition performance. In contrast, the interaction with water molecules remains relatively comparable for both systems, with slightly less negative values observed for PLA/ZnO (-81.97 kcal·mol^{-1}) than PLA (-84.61 kcal·mol^{-1}), suggesting a marginal reduction in water affinity.

Table 6
The adsorption energy calculated based on MC simulation.

Inhibitor	Adsorption Energy (E_{ads}) (Kcal. mol^{-1})	Rigid Adsorption Energy (Kcal. mol^{-1})	Deformation Energy (Kcal. mol^{-1})	Inh: dE_{ad}/dN_i (Kcal. mol^{-1})	H_2O: dE_{ad}/dN_i (Kcal. mol^{-1})
PLA	-4.56×10^3	-461.40	-4.11×10^3	-44.71×10^3	-84.61
PLA/ZnO	-4.42×10^6	-626.88	-4.4×10^6	-4.39×10^6	-81.97

3.6. Schematic illustration of the corrosion inhibition mechanism

The anticorrosion mechanism of the PLA/ZnO coating system on AA2024-T3 is schematically illustrated by comparing coatings incorporating unmodified ZnO nanoparticles with those containing surface

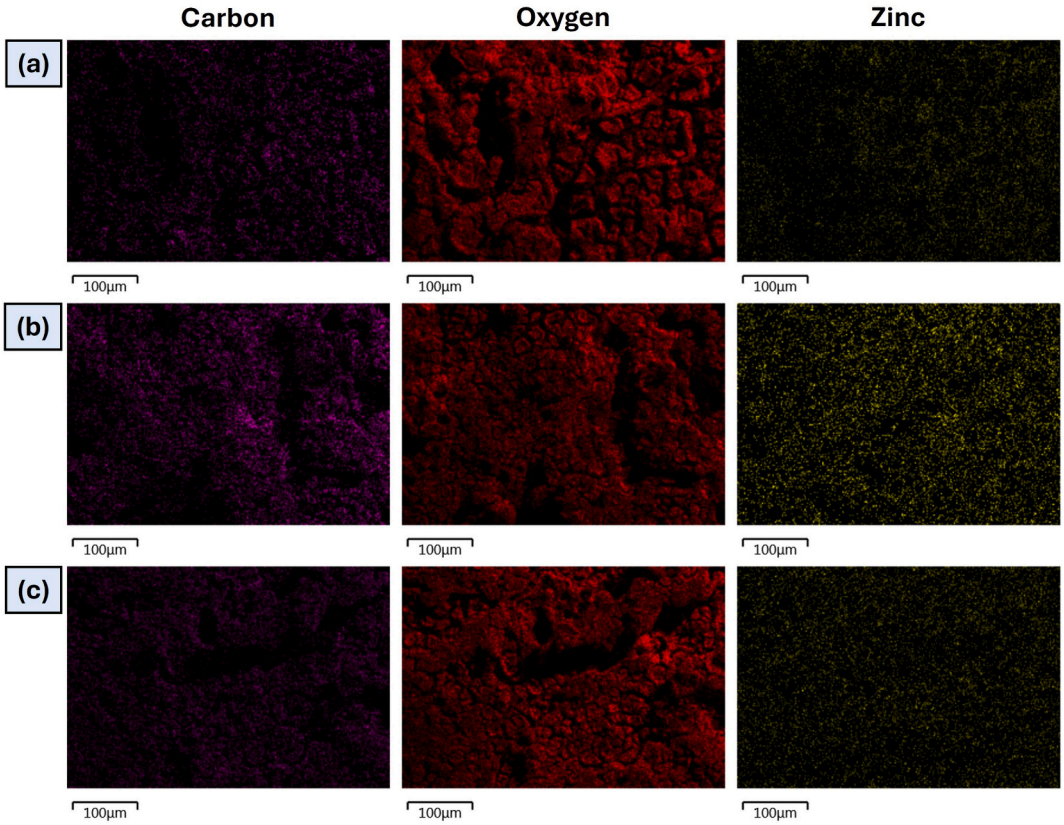

Fig. 9. EDX elemental mapping of carbon (C), oxygen (O), and zinc (Zn) for (a) PLA/ZnO, (b) PLA/ZnO/PEG, and (c) PLA/ZnO/CTAB coatings after immersion.

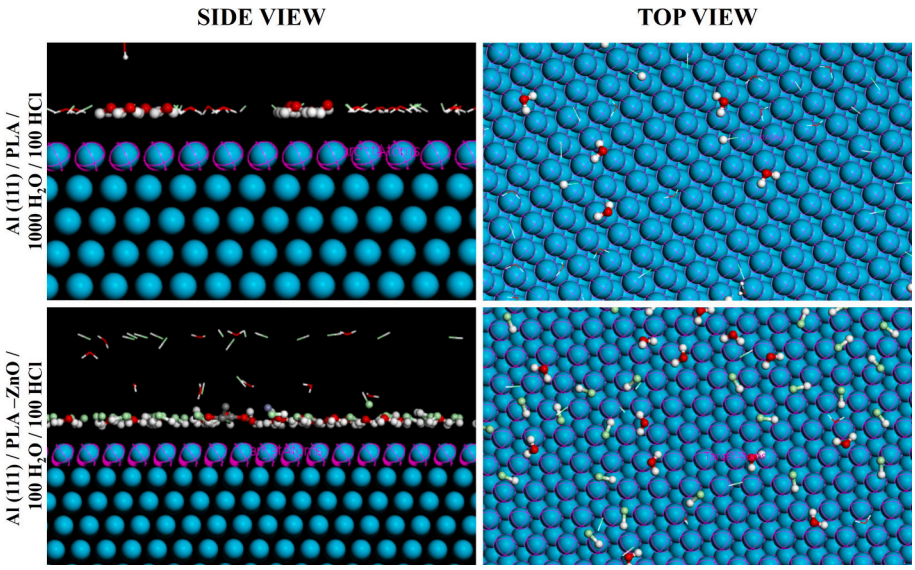

Fig. 10. The adsorption process of PLA and PLA/ZnO on aluminum alloy surface using MC simulation.

modified ZnO exhibiting a mesoporous architecture generated using surfactant templating agents, CTAB and PEG. In the coating containing unmodified ZnO NPs, the filler particles primarily act as passive physical barriers without providing effective regulation of aggressive species transport (Fig. 11a). Upon mechanical or environmental stress, the formation of micro cracks within the PLA matrix creates direct diffusion pathways, allowing Cl^-, OH^-, and H_2O molecules to rapidly penetrate the coating and reach the metal/coating interface. The direct interaction between these corrosive species and the AA2024-T3 substrate disrupts the native oxide film, accelerates localized electrochemical reactions, and ultimately promotes corrosion initiation and propagation.

ZnO NPs are surface modified using surfactants such as CTAB and PEG, a well-defined mesoporous ZnO structure is generated and uniformly dispersed within the PLA matrix. This mesoporous architecture fundamentally alters the corrosion protection mechanism of the coating [75,76]. When micro cracks form, aggressive ions do not directly reach the AA2024-T3 substrate; instead, they are preferentially captured, confined, and temporarily immobilized within the mesoporous channels of ZnO. The high specific surface area and interconnected pore network act as an ion buffering and diffusion regulating system, significantly prolonging the transport time of corrosive species (Fig. 11b).

As a result, the mesoporous ZnO creates a tortuous and energetically unfavorable diffusion pathway, effectively reducing the flux of Cl^-, OH^-, and water molecules toward the metal surface. This confinement effect minimizes the direct contact between corrosive species and the AA2024-T3 substrate, thereby suppressing anodic dissolution and cathodic reactions at the interface. Simultaneously, the improved dispersion of mesoporous ZnO enhances coating compactness and interfacial adhesion, limiting defect density and preventing crack propagation. The corrosion protection mechanism of the surface modified PLA/ZnO coating is governed not only by a conventional barrier effect but also by a mesopore-mediated ion trapping and diffusion retardation mechanism [59,77,78]. This synergistic effect effectively delays corrosion initiation, reduces electrochemical activity at the metal/coating interface, and significantly mitigates corrosion development on AA2024-T3. The proposed mechanism highlights the critical role of ZnO surface modification in transforming the coating from a passive barrier into an active corrosion mitigation system. The Monte Carlo simulation reveals a significant negative adsorption energy (4.42×10^6 kcal/mol), demonstrating that the localization of Cl^- ions within the mesopores is energetically favorable due to the confined space effect; this creates a robust diffusion barrier and a stabilized energy trap that effectively immobilizes the corrosive ions.

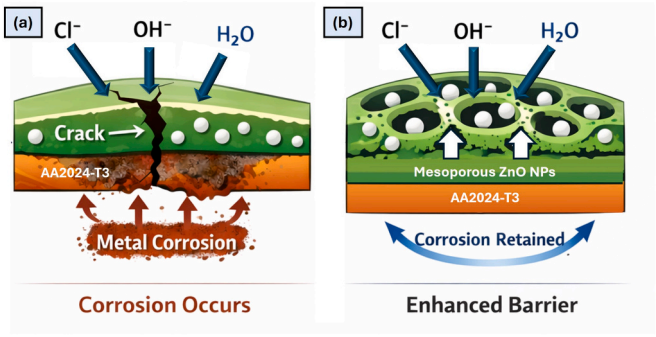

Fig. 11. Illustration of Corrosion inhibition mechanism on AA2024-T3 by (a) PLA/ZnO; (b) PLA/ZnO/CTAB or PLA/ZnO/PEG.

The results of this study highlight the strong potential of surfactant modified mesoporous ZnO nanoparticles as functional fillers in PLA coatings for chromate free corrosion protection of AA2024-T3. The enhanced anticorrosion performance is attributed to improved ZnO dispersion and mesoporous architectures that increase diffusion tortuosity and hinder the ingress of aggressive species. The present work is limited to static laboratory testing in a highly acidic medium with a single nanoparticle loading and does not address long term durability, cyclic exposure, or mechanical degradation. Future studies should therefore focus on evaluating performance under more realistic service environments, systematically optimizing mesoporous characteristics and filler content, and integrating inhibitor loaded mesoporous ZnO to achieve active or self-healing anticorrosion functionality.

4. Conclusion

This study demonstrates that surfactant-modified ZnO nanoparticles markedly enhance the anticorrosion performance of PLA-based coatings on AA2024-T3, with mesoporosity playing a decisive role in the protection mechanism. The incorporation of CTAB- and PEG-modified ZnO induced mesoporosity-driven structural modifications that improved nanoparticle dispersion, increased diffusion tortuosity, and reduced defect connectivity within the PLA matrix. As a result, the mesoporous ZnO effectively impeded the transport of aggressive species toward the metal/coating interface, thereby strengthening the barrier properties of the coating. The incorporation of surfactant-functionalized ZnO into the PLA matrix markedly enhances corrosion resistance in 1 M HCl. Among

the tested systems, PLA/ZnO/CTAB exhibits slightly superior inhibition performance (99.36% from Tafel analysis; 87.4% from EIS) compared to PLA/ZnO/PEG (99.31% Tafel; 85.3% EIS). Although the evaluation was limited to static laboratory conditions, these findings underscore the critical influence of mesoporosity on corrosion resistance and highlight the strong potential of PLA/mesoporous ZnO systems as environmentally benign, chromate-free alternatives for aerospace aluminum alloys.

CRediT authorship contribution statement

Budi Mulyati: Writing – review & editing, Writing – original draft, Formal analysis, Conceptualization. **Salma Nur Aisyah:** Validation, Investigation, Formal analysis, Data curation. **Saidun Fiddaroini:** Writing – review & editing, Writing – original draft, Visualization, Validation, Software. **Masruroh:** Visualization, Methodology, Formal analysis. **Ika Oktavia Wulandari:** Visualization, Supervision, Methodology. **Yuniar Ponco Prananto:** Supervision, Methodology. **Norhashila Hashim:** Writing – review & editing, Data curation. **Akhmad Sabarudin:** Writing – review & editing, Writing – original draft, Resources, Funding acquisition, Formal analysis, Data curation.

Declaration of competing interest

The authors declare that they have no known competing financial interests or personal relationships that could have appeared to influence the work reported in this paper.

Acknowledgement

This research was funded by the Directorate of Research and Community Service, Universitas Brawijaya, Indonesia, through the International Collaboration (C) Scheme 2025 (Grant No. 00741.8/UN10.A0501/B/PT.01.03.2/2025).

Declaration of generative AI and AI assisted technologies in the writing process

During the preparation of this work, the authors used ChatGPT to enhance the readability of the English text.

Data availability

Data will be made available on request.

References

[1] M. Merisalu, L. Aarik, J. Kozlova, H. Mändar, A. Tarre, V. Sammelselg, Effective corrosion protection of aluminum alloy AA2024-T3 with novel thin nanostructured oxide coating, Surf. Coat. Technol. 411 (2021) 126993, https://doi.org/10.1016/j.surfcoat.2021.126993.

[2] D. Georgoulis, C.M. Charalampidou, N. Siskou, N.D. Alexopoulos, S.K. Kourkoulis, Corrosion behaviour of AA2198–T8 and AA2024-T3 alloy in 3.5% aqueous solution, Procedia Struct. Integrity 28 (2020) 2297–2303, https://doi.org/10.1016/j.prostr.2020.11.076.

[3] O.D. Onukwuli, I.A. Nnanwube, F.O. Ochili, M. Omotioma, J.I. Obibuenyi, Corrosion inhibition effects of eco-friendly clarithromycin molecules on aluminium in hydrochloric acid solution via experimental, theoretical and optimization approach, Results Chem. 13 (2025) 101987, https://doi.org/10.1016/j.rechem.2024.101987.

[4] J. Christudasjustus, V.B. Vukkum, R.K. Gupta, Evolution of surface film in AA2024-T3 after a long-term immersion in NaCl solution, Corros. Sci. 215 (2023) 111056, https://doi.org/10.1016/j.corsci.2023.111056.

[5] D. Tobin, S. O'Shaughnessy, D. Trimble, Characterisation of force and torque with auxiliary heating during friction stir spot welding of AA2024-T3, Results Mater. 21 (2024) 100535, https://doi.org/10.1016/j.rinma.2024.100535.

[6] B. Shi, L. Wang, L. Qin, X. Guo, G. Yang, W. Wu, Z. Li, X. Cheng, Corrosion behavior of aluminum alloys in harsh marine atmospheric environment, Anti-Corrosion Methods Mater. 72 (2025) 761–775, https://doi.org/10.1108/ACMM-11-2024-3133.

[7] Margono, D.B. Darmadi, F. Gapsari, T.D. Widodo, B.M. Kartika, Enhanced corrosion resistance of aluminum 6061 alloy using Ti-based thin films and plasma nitriding, JCIS Open 18 (2025) 100139, https://doi.org/10.1016/j.jciso.2025.100139.

[8] B. Shri Prakash, J.N. Balaraju, Chromate (Cr6+)-free surface treatments for active corrosion protection of aluminum alloys: a review, J. Coat. Technol. Res. 21 (2024) 105–135, https://doi.org/10.1007/s11998-023-00831-1.

[9] Y. Zhigalenok, A. Tazhibayeva, S. Kokhmetova, A. Starodubtseva, T. Kan, D. Isbergenova, F. Malchik, Hexavalent chromium at the crossroads of science, environment and public health, RSC Adv. 15 (2025) 21439–21464, https://doi.org/10.1039/D5RA03104D.

[10] R. Mittal, A. Sharma, A.K. Bhardwaj, R. Bhateria, S. Bansal, R. Kashyap, S. Bhukal, Removal of chromium (VI) using spirulina assisted synthesized mesoporous iron oxide nanoparticles, Inorg. Chem. Commun. 154 (2023) 110881, https://doi.org/10.1016/j.inoche.2023.110881.

[11] J. Espinoza-Vergara, S. Gad, C.P. Silva, M.A. Paez, Z. Jin, Y. Xiong, M. Azocar, N. Vejar, C. Ramirez, X. Zhou, Covalent electrografting of aryl groups on AA2060-T8 surfaces, and their modification with Ce(4OHcin)3 to incorporate additional anticorrosive activity, J. Mater. Res. Technol. 31 (2024) 3014–3024, https://doi.org/10.1016/j.jmrt.2024.07.009.

[12] H. Zhu, J. Li, Advancements in corrosion protection for aerospace aluminum alloys through surface treatment, Int. J. Electrochem. Sci. 19 (2024) 100487, https://doi.org/10.1016/j.ijoes.2024.100487.

[13] M. Paz Martínez-Viademonte, S.T. Abrahami, T. Hack, M. Burchardt, H. Terryn, A review on anodizing of aerospace aluminum alloys for corrosion protection, Coatings 10 (2020) 1106, https://doi.org/10.3390/coatings10111106.

[14] J.W. Soedarsono, A. Andoko, K. Diharjo, F. Gapsari, S.M. Rangappa, S. Siengchin, Biodegradable PLA/HEC-ZNO nanocomposite for corrosion protection of ASTM a36 steel: a combined quantum and electrochemical analysis, Case Stud. Chem. Environ. Eng. 11 (2025) 101039, https://doi.org/10.1016/j.cscee.2024.101039.

[15] A.A. Gaber, H.K. Abd El-Hamid, R.E.A. Ngida, H.E.H. Sadek, R.M. Khattab, Synthesis, characterization and corrosive resistance of ZnO and ZrO2 coated TiO2 substrate prepared via polymeric method and microwave combustion, Ceram. Int. 50 (2024) 38917–38932, https://doi.org/10.1016/j.ceramint.2024.07.256.

[16] H. Bairagi, P. Vashishth, R. Sehrawat, S.K. Shukla, B. Mangla, Impact of novel ZnO/PAA nanocomposite as corrosion inhibitor on mild steel in 5% HCl, Mater. Chem. Phys. 315 (2024) 128958, https://doi.org/10.1016/j.matchemphys.2024.128958.

[17] D.C. Martínez Casillas, M.P. Longinotti, M.M. Bruno, F. Vaca Chávez, R.H. Acosta, H.R. Corti, Diffusion of water and electrolytes in mesoporous silica with a wide range of pore sizes, J. Phys. Chem. C 122 (2018) 3638–3647, https://doi.org/10.1021/acs.jpcc.7b11555.

[18] D.A. Mohammed, S.S. Al-Luaibi, H. Al-Sawaad, Synergistic corrosion inhibition of carbon steel in 1M HCl: a comprehensive of (polyaniline, polypyrrole, their copolymer)@NPs SiO2, Moroc. J. Chem. 12 (2024) 915–930, https://doi.org/10.48317/IMIST.PRSM/MORJCHEM-V12I2.46754.

[19] H. Byeon, J. Sunil, Exploring the novel environmentally friendly highly hydrophobic TiO2 coating for enhanced anti-corrosion performance of steel in potential industrial applications, Results Chem. 14 (2025) 102087, https://doi.org/10.1016/j.rechem.2025.102087.

[20] M. Tayyab, L. Zizhe, S. Rauf, Z. Xu, R.U.R. Sagar, F. Faiz, Z. Tayyab, R.U. Rehman, M. Imran, A. Waheed, R. Javed, A. Surulinathan, Z. Zafar, X.-Z. Fu, J.-L. Luo, Advanced fabrication techniques for polymer–metal nanocomposite films: state-of-the-art innovations in energy and electronic applications, Chem. Sci. 16 (2025) 3362–3407, https://doi.org/10.1039/D4SC04600E.

[21] J. Jomy, D. Prabhu, ZnO-functionalized arabinogalactan and xylan nanocomposite epoxy coating for the corrosion protection of AISI 5140 steel, J. Mol. Liq. 408 (2024) 125249, https://doi.org/10.1016/j.molliq.2024.125249.

[22] B. Mulyati, F. Gapsari, S. Fiddaroini, Masruroh, A. Sabarudin, PLA/ZnO nanocomposites with 0.05% w/v ZnO enhanced long-term corrosion inhibition of low carbon steel, S. Afr. J. Chem. Eng. 54 (2025) 397–417, https://doi.org/10.1016/j.sajce.2025.09.003.

[23] R. Abdel Hameed, M. Faride, M. Othman, B. Huwaimel, S. Al-Mhyawi, A. Shamroukh, F. Alshammary, E. Aljuhani, M. Abdallah, Green synthesis of zinc sulfide nanoparticles-organic heterocyclic polyol system as eco-friendly anti corrosion and anti-bacterial corrosion inhibitor for steel in acidic environment, Green Chem. Lett. Rev. 15 (2022) 847–862, https://doi.org/10.1080/17518253.2022.2141585.

[24] X. Dayu, L. Mingxing, K.R. Ansari, A. Singh, Synthesis of novel nano polymeric composite of zinc oxide and its application in corrosion inhibition of tubular steel in sweet corrosive medium, J. Mol. Liq. 359 (2022) 119327, https://doi.org/10.1016/j.molliq.2022.119327.

[25] N.B. Mahmood, F.R. Saeed, K.R. Gbashi, U.-S. Mahmood, Synthesis and characterization of zinc oxide nanoparticles via oxalate co-precipitation method, Mater. Lett.: X 13 (2022) 100126, https://doi.org/10.1016/j.mlblux.2022.100126.

[26] A. Rezaei, E. Katoueizadeh, S.M. Zebarjad, Investigation of the parameters affecting the morphology of zinc oxide (ZnO) nanoparticles synthesized by precipitation method, Mater. Today Chem. 26 (2022) 101239, https://doi.org/10.1016/j.mtchem.2022.101239.

[27] S. Rajan, A. Venugopal, H. Kozhikkalathil, S. Valappil, M. Kale, M. Mann, P. Ahuja, S. Munjal, Synthesis of ZnO nanoparticles by precipitation method: characterizations and applications in decipherment of latent fingerprints, Mater. Today Proc. (2023) S2214785323033151, https://doi.org/10.1016/j.matpr.2023.05.680.

[28] L. Zhang, X. Liu, J. Yan, Z. Li, S. Huang, Y. Weng, J. Li, C. Yuan, P. Han, S. Ye, X. Zhang, Preparation of superhydrophobic coating with anti-corrosion and anti-fouling properties on the surface of low manganese steel by electrodeposition, Surf. Coat. Technol. 460 (2023) 129412, https://doi.org/10.1016/j.surfcoat.2023.129412.

[29] N. Kühn, F. Frankenberg, A. Kwade, C. Schilde, Determination of interaction forces of (sub)-micron sized particles via the capillary rise method and colloidal probe atomic force microscopy: a combined approach, J. Colloid Interface Sci. 680 (2025) 696–713, https://doi.org/10.1016/j.jcis.2024.10.187.
[30] D. Kumar, A. Kumar, A. Kumar, R. Singh, M. Gautam, Effect of surfactant-assisted synthesis of ZnO nanoparticles on gas sensitivity, J. Electron. Mater. 54 (2025) 9631–9639, https://doi.org/10.1007/s11664-025-12398-1.
[31] Y. Xiong, M. Cao, Application of surfactants in corrosion inhibition of metals, Curr. Opin. Colloid Interface Sci. 73 (2024) 101830, https://doi.org/10.1016/j.cocis.2024.101830.
[32] M. Mobin, Huda, S. Zamindar, P. Banerjee, Mechanistic insight into adsorption and anti-corrosion capability of a novel surfactant-derived ionic liquid for mild steel in HCl medium, J. Mol. Liq. 385 (2023) 122403, https://doi.org/10.1016/j.molliq.2023.122403.
[33] Y. Rilda, R. Rinaldi, E.S. Putra, R. Refinel, A. Armaini, A. Agustien, A. Almurdi, H. Pardi, S. Jovita, A. Priyangga, E.P. Ramdhani, A novel approach revolutionizing ZnO nanoparticle synthesis with CTAB surfactant and spirulina palenthesis microalgae for enhanced antimicrobial performance, J. Dispers. Sci. Technol. (2025) 1–11, https://doi.org/10.1080/01932691.2024.2448454.
[34] A. Badry, A.A.E.H. Ibrahim, M.I. Said, A.A.E. Nasr, M.A. Mohamed, A.K. Hassan, M. M. Safwat, In vitro assessment of PEG-6000 coated-ZnO nanoparticles: modulating action to the resisted antibiotic activity against APEC, BMC Vet. Res. 19 (2023) 1, https://doi.org/10.1186/s12917-022-03562-4.
[35] U.P. Pamula, T.N. Rao, Y. Prashanthi, P. Ganji, Synthesis and characterization of ZnO@CTAB-SA polymer nanocomposites with biological and photocatalytic activity, Front. Nanotechnol. 7 (2025) 1674700, https://doi.org/10.3389/fnano.2025.1674700.
[36] F. Gapsari, S. Hadisaputra, A.M. Sulaiman, E. Ebenso, A. Thakur, A. Kumar, Eco-friendly corrosion inhibition of copper in NaCl media using perseana Americana extract: insights from quantum and electrochemical studies, Results Surf. Interfaces 17 (2024) 100327, https://doi.org/10.1016/j.rsurfi.2024.100327.
[37] M. Alharbi, R. Aslam, A. Khan, K.A. Alamry, M.A. Hussein, Y. Al-Hadeethi, E. Bekyarova, S. Alqahtani, Exploring corrosion protection of mild steel by ionic liquid functionalized graphene oxide: gravimetric, electrochemical, and surface studies, Results Chem. 13 (2025) 101985, https://doi.org/10.1016/j.rechem.2024.101985.
[38] B.M. Daas, P.Kr. Ghosh, B. Mandal, S. Ghosh, I. Basumallick, Electrochemical analysis of aluminium corrosion in alkaline battery fluid under the influence of alizarin red S and xylenol orange, Results Chem. 7 (2024) 101405, https://doi.org/10.1016/j.rechem.2024.101405.
[39] S. Mohan, M. Vellakkat, A. Aravind, R. U, Hydrothermal synthesis and characterization of zinc oxide nanoparticles of various shapes under different reaction conditions, Nano Ex. 1 (2020) 030028, https://doi.org/10.1088/2632-959X/abc813.
[40] A. Sanchooli, M. Karimipour, M. Molaei, Room temperature synthesis of au NR@Ag2S and Au NR@Ag2S/CdS core-shells using a facile photochemical approach, Phys. E. 109 (2019) 133–139, https://doi.org/10.1016/j.physe.2019.01.014.
[41] P. Sharma, S.K. Tiwari, P.B. Barman, Abnormal red shift in photoluminescence emission of ZnO nanowires, JOL 251 (2022) 119231, https://doi.org/10.1016/j.jlumin.2022.119231.
[42] F. Kleitz, W. Schmidt, F. Schüth, Calcination behavior of different surfactant-templated mesostructured silica materials, Microporous Mesoporous Mater. 65 (2003) 1–29, https://doi.org/10.1016/S1387-1811(03)00506-7.
[43] S. Mandal, C. Hazra, N. Joshi, N. Jain, P. Kumar, R. Sen, S. Das, K. Das, A comparison of chemical and biogenic surfactant mediated synthesis of ZnO/CuO: highlighting the antimicrobial activity of the bio-functionalized metal oxide nanoparticles, Colloids Surf. A Physicochem. Eng. Asp. 690 (2024) 133780, https://doi.org/10.1016/j.colsurfa.2024.133780.
[44] N.J. A, A. P, N. R, M. S, Low temperature-based ceria-ZnO nanocomposites for ammonia gas sensors: effect of surfactant on physicochemical properties of ZnO nanostructures, Mater. Sci. Semicond. Process. 204 (2026) 110271, https://doi.org/10.1016/j.mssp.2025.110271.
[45] M.D. Fite, A.L. Berhanu, A comprehensive review on the effect of zinc salt precursors for synthesis, characterization, and applications of ZnO nanoparticles, Nano-Struct. Nano-Objects 43 (2025) 101529, https://doi.org/10.1016/j.nanoso.2025.101529.
[46] R. Bharadwaj, M. R, S.D. K R, D. Pinheiro, S. Manickam, Enhancing photocatalytic performance through surfactant-assisted electrochemical synthesis: surface modification of hierarchical ZnO morphologies with Ag/ZnWO4 nanoparticles, J. Mol. Struct. 1306 (2024) 137835, https://doi.org/10.1016/j.molstruc.2024.137835.
[47] L. Qomariyah, T. Hirano, N.R. Putra, S. Suprapto, H.A. Ajiz, M. Fauziyah, Innovative surfactant-free synthesis of core–shell SiO2 /ZnO particles: rapid ultrasonication and photocatalytic inhibition, RSC Adv. 14 (2024) 12665–12675, https://doi.org/10.1039/D4RA01309C.
[48] X. Sun, Y. Meng, K. Hu, J. Sun, C. Zhou, C. Su, L. Zhang, C. Zhang, Z. Ma, Crystallization-driven formation of cluster assemblies on surface for super-hydrophobic poly (L-lactic acid)/ZnO composite membrane, Int. J. Biol. Macromol. 283 (2024) 137815, https://doi.org/10.1016/j.ijbiomac.2024.137815.
[49] C. Sotelo-Vazquez, C. Sanchez-Perez, D.I. De La Fuente Rodríguez, J. Marugán, Nanostructured ZnO coatings as antiviral surfaces: influence of synthesis methodology on photocatalytic efficiency, J. Environ. Chem. Eng. 13 (2025) 120195, https://doi.org/10.1016/j.jece.2025.120195.
[50] J. Soli, S. Kachbouri, E. Elaloui, C. Charnay, Role of surfactant type on morphological, textural, optical, and photocatalytic properties of ZnO nanoparticles obtained by modified sol–gel, J. Sol-Gel Sci. Technol. 100 (2021) 271–285, https://doi.org/10.1007/s10971-021-05653-4.
[51] M. Bazari, N. Najmoddin, The effect of cationic, anionic and nonionic surfactants on morphology and antibacterial properties of zinc oxide, Matéria (Rio J) 27 (2022) e13172, https://doi.org/10.1590/s1517-707620220002.1372.
[52] M. Panigrahi, Chemically synthesized ZnO nanostructure: effect of polyethylene glycol (PEG) surfactants, NanoNEXT 3 (2022) 6–13, https://doi.org/10.54392/nnxt2232.
[53] Y. Zhang, L. Tao, C. Xie, D. Wang, Y. Zou, R. Chen, Y. Wang, C. Jia, S. Wang, Defect engineering on electrode materials for rechargeable batteries, Adv. Mater. 32 (2020) 1905923, https://doi.org/10.1002/adma.201905923.
[54] P.A. Dash, S. Mohanty, S.K. Nayak, Synthesis and characterization of ZnO/MgO doped mesoporous bioactive glass: enhanced bioactivity and antibacterial properties for bone tissue engineering applications, Ceram. Int. 51 (2025) 38129–38140, https://doi.org/10.1016/j.ceramint.2025.06.049.
[55] K.S. Mohammed, M. Atlabachew, G.W. Derbie, B.A. Berhie, Nano modified kaolin-based materials and their application: a review, JCIS Open 20 (2025) 100153, https://doi.org/10.1016/j.jciso.2025.100153.
[56] J. Wang, X. Zhao, G. Zou, L. Zhang, S. Han, Y. Li, D. Liu, C. Fernandez, L. Li, L. Ren, Q. Peng, Crystal-defect engineering of electrode materials for energy storage and conversion, Mater. Today Nano 22 (2023) 100336, https://doi.org/10.1016/j.mtnano.2023.100336.
[57] J. Chen, X. Yan, Z. Geng, M.X. Zhang, C.W. An, The effect of surfactants on FOX-7 crystals, Mater. Today Commun. 46 (2025) 112817, https://doi.org/10.1016/j.mtcomm.2025.112817.
[58] T. Mao, X. Shi, M. Liu, Q. Su, Y. Cheng, C. Fang, X. Luo, Study on pore size distribution method of SBA-15 in polymer composites, Mater. Today Commun. 35 (2023) 105592, https://doi.org/10.1016/j.mtcomm.2023.105592.
[59] Y. Hao, E. Duan, J. Long, L. Song, Y. Shen, S. Liu, Anticorrosion mechanism of epoxy coating containing mesoporous resorcinol-formaldehyde hollow nanosphere loaded with 8-Hydroxyquinolin, Appl. Surf. Sci. 677 (2024) 161014, https://doi.org/10.1016/j.apsusc.2024.161014.
[60] Y. Ahmadi, R. Nazari, M. Mansouri, Enhanced oil recovery using a green nanocomposite with cetyltrimethylammonium bromide and sodium dodecyl sulfate surfactants in sandstone reservoir, Phys. Fluids 37 (2025) 076112, https://doi.org/10.1063/5.0271067.
[61] A.D. Drozdov, J.deC. Christiansen, Micromechanical modeling of barrier properties of polymer nanocomposites, Compos. Sci. Technol. 189 (2020) 108002, https://doi.org/10.1016/j.compscitech.2020.108002.
[62] S. Xiong, D. Liang, High-temperature diffusion behavior, wear-resistance and corrosion-resistance properties of Al2O3, MoS2, and ZnO nanoparticles on copper surfaces, Surf. Interfaces 58 (2025) 105840, https://doi.org/10.1016/j.surfin.2025.105840.
[63] X. Jin, J. Wang, S. Zheng, J. Li, X. Ma, L. Feng, H. Zhu, Z. Hu, The study of surface activity and anti-corrosion of novel surfactants for carbon steel in 1 m HCl, J. Mol. Liq. 353 (2022) 118747, https://doi.org/10.1016/j.molliq.2022.118747.
[64] S. Suhartini, N.A. Rohma, A.P. Agus Pratama, N.M. Sabrina Sunyoto, E. Mardawati, Kasbawati, A.M. Sulaiman, A. Harmayanti, F. Gapsari, Sustainable corrosion protection: chitosan/reduced graphene oxide nanocomposite coating derived from palm oil empty fruit bunches on low carbon steel, Case Stud. Chem. Environ. Eng. 11 (2025) 101116, https://doi.org/10.1016/j.cscee.2025.101116.
[65] Y. Huang, C. Zhao, Y. Li, C. Wang, T. Shen, C. Wu, Z. Hu, D. Cheng, H. Yang, Enhanced corrosion resistance and self-healing effect of sol–gel coating incorporating one-pot-synthesized corrosion inhibitor-encapsulated silica nanocontainers, J. Sol-Gel Sci. Technol. 104 (2022) 78–90, https://doi.org/10.1007/s10971-022-05929-3.
[66] Y. Zhang, J. Xing, H. Tian, L. Liu, J. Qian, Smart nanoarchitectonics of epoxy coating: preparation, release behavior and self-healing performance based on mesoporous silica nano-containers loaded with DMTD inhibitors, Mater. Today Commun. 39 (2024) 108673, https://doi.org/10.1016/j.mtcomm.2024.108673.
[67] C. Zhang, W. Li, Z. Guo, T. Sun, W. Wang, S. Chen, Controllable construction of mesoporous silica/2D-COF nanocomposites reinforced epoxy coatings with excellent self-repairing and long-lasting anticorrosion performances, Prog. Org. Coat. 177 (2023) 107441, https://doi.org/10.1016/j.porgcoat.2023.107441.
[68] Y. Albarqouni, E. Banius, N.H. Abu Bakar, A. Abdullah, Enhancing epoxy coatings with spherical ZnO nanoparticles for improved hydrophobicity and corrosion resistance, J. Adhes. Sci. Technol. 39 (2025) 3009–3029, https://doi.org/10.1080/01694243.2025.2526006.
[69] M. Shakourian, S. Rahemi Ardekani, A. Bayat, E. Saievar-Iranizad, W. Deferme, Ultrasonic atomization based fabrication of superhydrophobic and corrosion-resistant hydrolyzed MTMS/PVDF coatings, JCIS Open 7 (2022) 100059, https://doi.org/10.1016/j.jciso.2022.100059.
[70] Sh. Ammar, K. Ramesh, B. Vengadaesvaran, S. Ramesh, A.K. Arof, Amelioration of anticorrosion and hydrophobic properties of epoxy/PDMS composite coatings containing nano ZnO particles, Prog. Org. Coat. 92 (2016) 54–65, https://doi.org/10.1016/j.porgcoat.2015.12.007.
[71] H. Chen, H. Fan, N. Su, R. Hong, X. Lu, Highly hydrophobic polyaniline nanoparticles for anti-corrosion epoxy coatings, Chem. Eng. J. 420 (2021) 130540, https://doi.org/10.1016/j.cej.2021.130540.
[72] X. Gong, S. He, Highly durable superhydrophobic polydimethylsiloxane/silica nanocomposite surfaces with good self-cleaning ability, ACS Omega 5 (2020) 4100–4108, https://doi.org/10.1021/acsomega.9b03775.
[73] S. Faisal, H. Jan, S.A. Shah, S. Shah, A. Khan, M.T. Akbar, M. Rizwan, F. Jan, Wajidullah, N. Akhtar, A. Khattak, S. Syed, Green synthesis of zinc oxide (ZnO) nanoparticles using aqueous fruit extracts of *Myristica fragrans*: their

characterizations and biological and environmental applications, ACS Omega 6 (2021) 9709–9722, https://doi.org/10.1021/acsomega.1c00310.
[74] Y. Liang, Y. Yuan, B. Wang, Y. Wang, S. Wei, Microstructure and microwave absorption properties of ZnO with different surfactants by hydrothermal method, J. Mater. Sci. Mater. Electron. 32 (2021) 25908–25918, https://doi.org/10.1007/s10854-020-05226-1.
[75] H. Zheng, Y. Xu, J. Huang, X. Zhu, H. Zhang, H. Zhang, J. Zhu, Self-healing anti-corrosion powder coatings via PDMS-infiltrated mesoporous silica, Appl. Surf. Sci. 721 (2026) 165357, https://doi.org/10.1016/j.apsusc.2025.165357.
[76] M. Agheli, M.R. Vaezi, B. Aghabarari, B. Ramezanzadeh, Integrating PANI@BTA@MSN mesoporous nano-hybrid into zinc-rich epoxy coatings for long-term smart anti-corrosion durability, Prog. Org. Coat. 205 (2025) 109329, https://doi.org/10.1016/j.porgcoat.2025.109329.
[77] Y. Hao, Y. Shen, L. Song, E. Duan, S. Liu, Anticorrosion mechanism of mesoporous polyaniline hollow nanosphere loaded with 8-HQ in an epoxy coating for aluminum alloy, Constr. Build. Mater. 466 (2025) 140293, https://doi.org/10.1016/j.conbuildmat.2025.140293.
[78] T.T. Thai, M.-E. Druart, Y. Paint, A.T. Trinh, M.-G. Olivier, Influence of the sol-gel mesoporosity on the corrosion protection given by an epoxy primer applied on aluminum alloy 2024 –T3, Prog. Org. Coat. 121 (2018) 53–63, https://doi.org/10.1016/j.porgcoat.2018.04.013.